J Therm Anal Calorim (2015) 122:653–663
DOI 10.1007/s10973-015-4778-7

Synthesis of rambutan-like $MnCo_2O_4$ and its adsorption performance for methyl orange

Kaituo Wang[1] · Xuehang Wu[1] · Wenwei Wu[1,2] · Wen Chen[1] · Liqin Qin[1] · Xuemin Cui[1]

Received: 20 September 2014 / Accepted: 9 May 2015 / Published online: 3 June 2015

Abstract A hierarchical rambutan-like $MnCo_2O_4$ precursor is synthesized by a co-precipitation method in water–ethanol at room temperature. After being calcined at 400 °C in air for 10 min with a heating rate of 1 °C min^{-1}, the precursor $MnCo_2(C_2O_4)_3{\cdot}5.54H_2O$ is transformed into the rambutan-like $MnCo_2O_4$ microspheres composed of end-connected nanorods, which has a large specific surface area (155 $m^2\ g^{-1}$). When evaluated as adsorbent for methyl orange (MO), the rambutan-like $MnCo_2O_4$ microspheres show excellent adsorption ability for methyl orange. The adsorption capacity of methyl orange on rambutan-like $MnCo_2O_4$ is 185.14 mg g^{-1} under the conditions of initial MO concentration 12 mg L^{-1} and pH 2.09. Adsorption kinetics of methyl orange on rambutan-like $MnCo_2O_4$ follows the pseudo-second-order kinetic model. The values of adsorption activation energy E_a and enthalpy $\Delta H^{\#}$ are 5.71 ± 0.056 and 9.30 kJ mol^{-1}, respectively. Methyl orange adsorption on rambutan-like $MnCo_2O_4$ is an endothermic and physical adsorption process.

Keywords Rambutan-like $MnCo_2O_4$ · Chemical synthesis · Methyl orange · Adsorption kinetics

✉ Wenwei Wu
gxuwuwenwei@aliyun.com; wuwenwei@gxu.edu.cn

[1] School of Chemistry and Chemical Engineering, Guangxi University, Nanning 530004, People's Republic of China

[2] Guangxi Colleges, Universities Key Laboratory of Applied Chemistry Technology and Resource Development, Nanning 530004, People's Republic of China

Introduction

Nowadays, many kinds of dyes are being used in many fields including textile, tannery, electroplating, food processing, and papermaking. At the same time, a large amount of highly colored effluents are released into the environment, probably containing more than 100,000 kinds of commercial dyes and over 7 million tons annually [1–5], which will cause serious environmental problems. Among dyes, azo dyes are mostly used, which contain an azo group (–N=N–) as part of the structure. Although azo dyes are not strongly toxic, they can cause serious damage because these dyes prevent sunlight and oxygen penetration and then have a derogatory effect on photosynthetic activity in aquatic systems [6]. The azo dyes are very stable against heat, light, and many chemicals. Therefore, it is very difficult to remove these dyes from wastewater by sunniness, chemical, and biological degradation methods. Methyl orange (MO) is a kind of azo dye which has been widely used in many fields. Removal of MO at a low cost is still a significant challenge.

Various conventional methods have been developed to treat wastewater including coagulation–flocculation [7], membrane separation [8], photocatalytic degradation [9], and adsorption [10–17]. Among the traditional wastewater treatment process techniques, adsorption technique has been considered to be a convenient and effective wastewater treatment technique due to simplicity, low cost, and insensitivity to toxic substances [18]. To date, various adsorbents, such as nanoporous silica, hematite, MnO–Fe_2O_3, $CuFe_2O_4$, Fe_2O_3–SiO_2, mesoporous TiO_2, and activated carbon and/or mesoporous carbon, have been investigated to remove azo dyes from wastewater. Activated carbon and/or mesoporous carbon have large specific surface area, so they are efficient adsorbents for organic compounds.

However, activated carbons and mesoporous carbon cannot be reused, resulting in high cost, and limited its large-scale application.

A practical adsorbent must meet the following conditions: (1) high adsorption capacity; (2) adsorbent is easily separated from the solution after adsorption; (3) adsorbent can be repeatedly used after simple processing. Obviously, magnetic materials could satisfy the requirements above because they have high adsorption capacity, and can be easily separated from treated water under an external magnetic field and repeatedly used after simple processing. Spinel ferrites (MFe_2O_4, M = transition metal and/or alkaline earth metal) behave with ferromagnetic property at room temperature. So, they have been widely used as the magnetic carrier in adsorbent to realize magnetic separation [19, 20]. To date, various spinel ferrites have used as adsorbents to treat wastewater containing dyes, including $ZnFe_2O_4$ [21], $CuFe_2O_4$ [22], $NiFe_2O_4$ [23], $MnFe_2O_4$ [24], $CoFe_2O_4$ [25], $ZnCr_2O_4$ [26], and Fe_3O_4 [27]. However, the adsorption capacity of ferrites is far lower than that of the activated carbon in recent reports due to small specific surface area of ferrites. Therefore, synthesis of ferrites with high surface area is the key to improve the adsorption capacity of ferrites. It was reported that ferrite with 3D porous structure could have high efficient adsorption property due to its large specific surface area [23].

$MnCo_2O_4$ is a very important mixed metal oxide with an inverse spinel structure and magnetic property. The quality of $MnCo_2O_4$ powders strongly depends on the synthesis method and conditions, which determine particle size, morphology, specific surface area, lattice parameters, stoichiometry, and average Mn valence of $MnCo_2O_4$ associated with adsorption, catalytic, and electrochemical performances [28–30]. Preparations of high-quality samples with unique three-dimensional structure and/or large surface area have generally been considered to be very helpful to improve adsorption, catalytic, and electrochemical performances of $MnCo_2O_4$. To the best of our knowledge, adsorption performances of hierarchical rambutan-like $MnCo_2O_4$ have rarely been reported in previous studies.

In this paper, we report a facile and scalable approach to fabricate hierarchical rambutan-like $MnCo_2O_4$ with large specific surface area. It is worth mentioning that the unique architecture is obtained via a self-assembly process without any additional templates. Investigations on adsorption properties of rambutan-like $MnCo_2O_4$ as adsorbent for methyl orange were performed. The results show that the rambutan-like $MnCo_2O_4$ is easily separated from the solution after adsorption under an external magnetic field. More important, the adsorption capacity of methyl orange (185.14 mg g^{-1}) on this rambutan-like $MnCo_2O_4$ is very high. It is expected to be a promising reusable adsorbent. The adsorption kinetics of methyl orange on rambutan-like $MnCo_2O_4$ was interpreted by the pseudo-first- and second-order rate equations [23, 31, 32]. The adsorption activation energy E_a and mechanisms of methyl orange on the rambutan-like $MnCo_2O_4$ are discussed in this paper for the first time.

Experimental

Reagent and apparatus

All chemicals used are of reagent-grade purity (purity > 99.9 %). The thermogravimetry (TG) measurement was conducted using a Netzsch STA 409 PC/PG thermogravimetric analyzer under continuous flow of O_2 (30 mL min^{-1}). The sample mass was approximately 13 mg. X-ray powder diffraction (XRD) was performed using a Rigaku D/Max 2500 V diffractometer equipped with a graphite monochromator and a Cu target. The radiation applied was Cu Kα ($\lambda = 0.15406$ nm), operated at 40 kV and 50 mA. The XRD scans were conducted from 5° to 70° in 2θ, with a step size of 0.02°. The morphologies of the synthesis products were observed using a S-3400 scanning electron microscope (SEM). The nitrogen adsorption and desorption isotherms were measured at 77 K on a Micromeritics Tristar 3020 analyzer. The IR spectra of the rambutan-like $MnCo_2O_4$ before and after adsorption of MO were recorded on a Nexus 470 Fourier transform IR (FT-IR) instrument. Zeta potential was analyzed by DLS (ELS-Z, Photal).

Preparation of $MnCo_2O_4$

The rambutan-like $MnCo_2O_4$ precursor was prepared by a co-precipitation method in water–ethanol solution at room temperature [33]. In a typical synthesis, 60 mL of 0.1 M $MnSO_4$ aqueous solution, 120 mL of 0.1 M $CoSO_4$ aqueous solution, and 180 mL of ethanol (C_2H_5OH) were mixed for 5 min at room temperature at first. After that, 185 mL of 0.1 M $Na_2C_2O_4$ solution was quickly poured into the above solution under magnetic stirring. The reaction mixture was kept at room temperature for 2.5 h. The pink precipitate was collected by filtration, washed with deionized water, and dried at 60 °C for 6 h. The resulting precursor was determined to be $MnCo_2(C_2O_4)_3{\cdot}5.54H_2O$. Finally, with a slow heating rate of 1 °C min^{-1}, the precursor was further treated at 400, 450, and 550 °C for 10 min in air to produce the rambutan-like $MnCo_2O_4$ microspheres, respectively.

Adsorption kinetic experiments

Adsorption experiments were carried out in a 200-mL beaker containing 6 mg $MnCo_2O_4$ powders and 100 mL methyl orange solutions. The beaker was placed in a thermostat oil bath at a stirring speed of 300 rpm and desired temperature (±1 °C). The pH value of methyl orange solution was adjusted with sulfuric acid solution. The effect of initial concentration on methyl orange adsorption kinetics was studied by varying initial methyl orange concentration from 4.5 to 12 mg L^{-1} (4.5, 6, and 12 mg L^{-1}) at temperature of 284 K. While to study the effect of temperature on methyl orange adsorption kinetics, experiments were performed at temperature of 284, 314, and 324 K with 6 mg L^{-1} methyl orange initial concentration. The contact time intervals (5, 10, 15, 20, and 30 min) were adopted to obtain adsorption kinetic data. The supernatant liquid in the beaker was separated from adsorbent by filtration, and the filtrate was collected for analysis. Methyl orange concentration in this study was measured based on spectrophotometry. The adsorption amount of methyl orange on rambutan-like $MnCo_2O_4$ at time t, q_t (mg g^{-1}), was calculated using the following formula (Eq. 1):

$$q_t = \frac{(C_0 - C_t) \times V}{m} \tag{1}$$

where C_o (mg L^{-1}) and C_t (mg L^{-1}) are the initial and the current methyl orange concentration at time t, respectively, V (mL) is the volume of the adsorption solution, and m (mg) is the mass of rambutan-like $MnCo_2O_4$.

Method of determining adsorption activation energy and adsorption kinetic models

Kinetics of adsorption process was interpreted by the pseudo-first- and second-order rate equations, which have been widely used for adsorption study of pollutants from wastewater in recent years [23, 34, 35].

The pseudo-first-order equation can be expressed as Eq. (2):

$$\frac{dq_t}{dt} = k_{p1}(q_e - q_t) \tag{2}$$

Equation (2) can be rewritten into Eq. (3):

$$\log(q_e - q_t) = \log q_e - \frac{k_{p1}}{2.303} \times t \tag{3}$$

The dependence of $\log(q_e - q_t)$ on t must lead to a straight line. Thus, rate constant of the adsorption process (k_{p1}, 1/min) can be obtained from linear slope [$-k_{p1}/2.303$, Eq. (3)].

The pseudo-second-order equation can be expressed as follows:

$$\frac{dq_t}{dt} = k_{p2}(q_e - q_t)^2 \tag{4}$$

where k_{p2} (g mg^{-1} min^{-1}) is the pseudo-second-order rate constant of adsorption process [36]. The integral form of Eq. (4) with boundary conditions $t = 0$ to $t = t$, and $q_t = 0$ to $q_t = q$ can be expressed as Eq. (5):

$$\frac{1}{(q_e - q_t)} = \frac{1}{q_e} + k_{p2} \times t \tag{5}$$

By a series of transforms, thus Eq. (5) can be rewritten as Eq. (6):

$$\frac{1}{q_t} = \frac{1}{q_e} + \frac{1}{k_{p2}q_e^2} \times \frac{1}{t} \tag{6}$$

Dependence of $1/q_t$ on $1/t$ should be a straight line if the adsorption kinetics follows the pseudo-second-order rate equation. Thus, the rate constant of the adsorption process (k_{p2}) can be obtained from linear slope [$1/k_{p2}q_e^2$, Eq. (6)]. Equations (3) and (6) will be used to fit the adsorption kinetic data of methyl orange on rambutan-like $MnCo_2O_4$.

The adsorption activation energy (E_a) can be calculated using Arrhenius equation [Eq. (7)]:

$$\ln k = -\frac{E_a}{RT} + \ln A \tag{7}$$

where k is the rate constant of the adsorption process, E_a is the activation energy (kJ mol^{-1}), A is the pre-exponential factor, R is the gas constant (8.314 × 10^{-3} kJ mol^{-1} K^{-1}), and T is adsorption temperature (K). The dependence of ln k on $1/T$ must lead to a straight line. Thus, the adsorption activation energy E_a can be obtained from linear slope [$-E_a/R$, Eq. (7)].

Entropy ($\Delta S^{\#}$), enthalpy ($\Delta H^{\#}$), and Gibbs energy (free enthalpy) ($\Delta G^{\#}$) of the adsorption process were calculated using Eyring equations [37, 38]:

$$\Delta S^{\#} = R\left[\ln\left(\frac{hA_\alpha}{k_B T_\alpha} - 1\right)\right] \tag{8}$$

$$\Delta H^{\#} = E_{a,\alpha} - RT_\alpha \tag{9}$$

$$\Delta G^{\#} = \Delta H^{\#} - T_\alpha \Delta S^{\#} \tag{10}$$

Results and discussion

Composition analysis of the precursor

0.0295 g precursor sample was dissolved in 10 mL 50 vol% HCl solution and then diluted to 100.00 mL with deionized water. Manganese (Mn) and cobalt (Co) in the

solution were determined by inductively coupled plasma atomic emission spectrometry (ICP-AES, Perkin Elmer Optima 5300 DV). The results showed that the Mn and Co mass percentages were 10.20 and 22.00 %, respectively. In other words, molar ratio of Mn:Co in the precursor was 1.000:2.01, which was close to the value of the pre-design and synthesis.

TG/DTG analysis of the precursor

Figure 1 shows the TG/DTG curves of the precursor at a heating rate of 10 °C min^{-1}. The TG/DTG curves show that the thermal process of $MnCo_2(C_2O_4)_3{\cdot}5.54H_2O$ below 600 °C occurred in two well-defined steps. The first step started at about 50 °C and ended at 175 °C, which can be attributed to the dehydration of the 5.54 waters from $MnCo_2(C_2O_4)_3{\cdot}5.54H_2O$ (mass loss: observed, 18.32 %; theoretical, 18.60 %). The second thermal process step started at 175 °C and ended at 307 °C, attributed to the reaction of $MnCo_2(C_2O_4)_3$ with $2O_2$ into $MnCo_2O_4$ and the six CO_2 molecules (mass loss: observed, 37.56 %; theoretical, 37.28 %).

X-ray powder diffraction and particle distribution characterization

Figure 2 shows the XRD patterns of the samples calcined at different temperatures. All the diffraction peaks in the pattern can be indexed to cubic $MnCo_2O_4$ with space group Fd-3 m (227) (PDF card No. 23-1237). No impurity peaks are detected, revealing the high purity of the as-synthesized samples.

The crystallite diameter of $MnCo_2O_4$ was estimated using the following Scherrer formula [39, 40]:

$$D = K\lambda/(\beta\cos\theta) \quad (11)$$

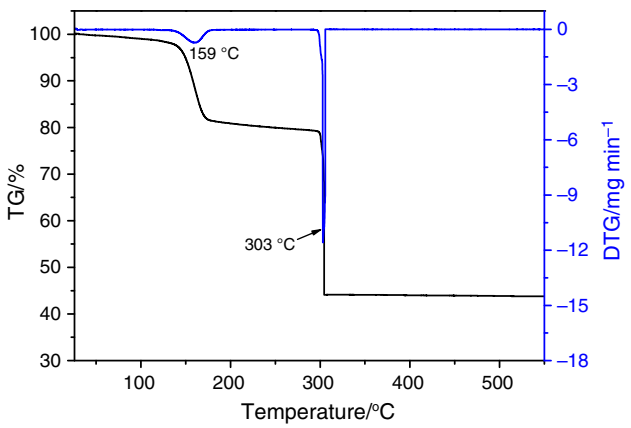

Fig. 1 TG/DTG curves of $MnCo_2(C_2O_4)_3{\cdot}5.54H_2O$ at a heating rate of 10 °C min^{-1} in O_2

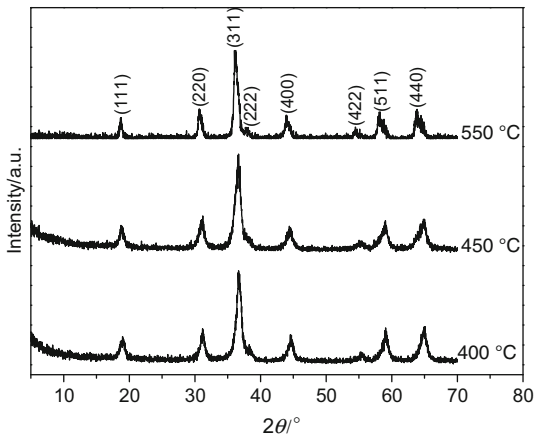

Fig. 2 XRD patterns of $MnCo_2O_4$ at different temperatures for 10 min

where D is the crystallite diameter, $K = 0.89$ (the Scherrer constant), $\lambda = 0.15406$ nm (wavelength of the X-ray used), β is the width of line at the half-maximum intensity, and θ is the corresponding angle. The crystallite sizes of $MnCo_2O_4$ from calcining the precursor at 400, 450, and 550 °C are 9.5, 9.6, and 12.6 nm, respectively. The crystallinity of $MnCo_2O_4$ can be calculated by MDI Jade 5.0 software. The crystallinity of $MnCo_2O_4$ obtained at 400, 450, and 550 °C was approximately 100 %.

Figure 3 shows SEM images of the $MnCo_2O_4$ synthesized at 400, 450, and 550 °C, respectively. It is found that all the as-synthesized $MnCo_2O_4$ samples exhibit uniform rambutan-like microspheres with a size of about 4.3 μm, which are composed of many end-connected nanorods. In Fig. 3a, b, the diameter of nanorods in the sample obtained at 400 and 450 °C is about 80 nm. By contrast, after being calcined at 550 °C, the nanorods become thicker and shorter but the hierarchical structure is able to be well preserved without obvious deformation (Fig. 3c).

The nitrogen adsorption–desorption isotherms of the samples calcined at different temperatures (400, 450, and 550 °C) are shown in Fig. 4. All these isotherms exhibit a typical type IV characteristic with an obvious hysteresis loop, indicating the mesoporous structures in the samples [41]. Owing to the nanorod subunits and the presence of the void spaces between them, the measured values of the BET surface areas reach 155, 126, and 43 $m^2\ g^{-1}$ for 400, 450, and 550 °C, respectively, which are much higher than those of $MnCo_2O_4$ microspheres and $MnCo_2O_4$ nanowires [42, 43]. The specific surface area is highly dependent on the calcination temperature. With the increase in the calcination temperature, the aggregation of primary nanoparticles also increases, resulting in a significant decrease in specific surface area. The facile fabrication process and a unique three-dimensional structure will make the as-synthesized samples possible to be applied in adsorption and other relevant fields.

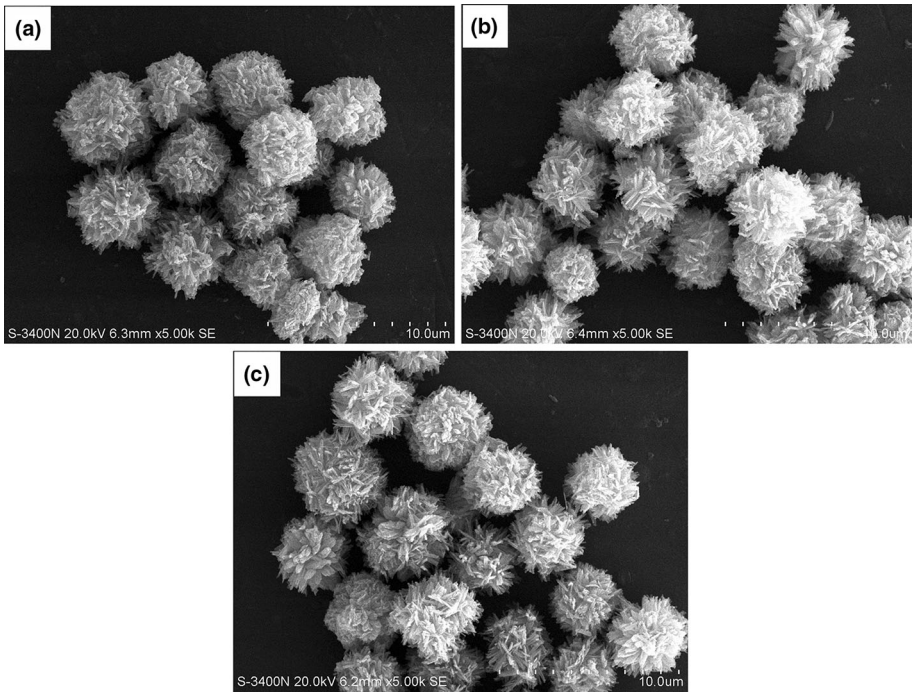

Fig. 3 SEM images of the calcined samples at different temperatures for 10 min: **a** 400 °C, **b** 450 °C, and **c** 550 °C

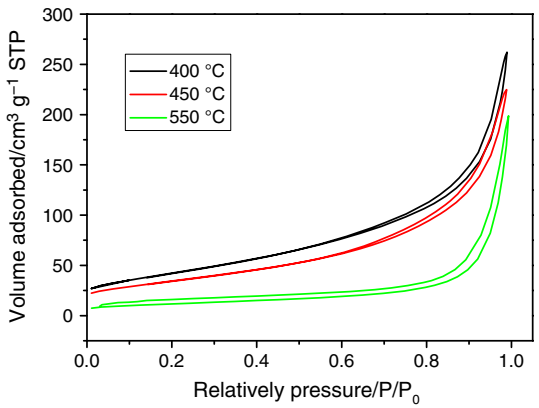

Fig. 4 Nitrogen adsorption and desorption isotherms of rambutan-like $MnCo_2O_4$

For sample synthesized by co-precipitation method in this study, rambutan-like $MnCo_2O_4$ nanocrystals showed superparamagnetic behavior. Figure 5 shows that the rambutan-like $MnCo_2O_4$ powder can be easily separated from the aqueous solution after adsorption with a permanent magnet.

IR spectroscopic analyses of the rambutan-like $MnCo_2O_4$ microspheres before and after adsorption of MO

The FT-IR spectra of MO and the rambutan-like $MnCo_2O_4$ microspheres before and after adsorption are shown in Fig. 6. Bands at 3354 and 2930–2900 cm^{-1} were attributed to the stretching vibration of –OH and the stretching vibration or the asymmetric stretching vibration of $–CH_3$, respectively. The bands located at the wavenumber ranges of 1600–1400 and 910–720 cm^{-1} were assigned to the C=C stretching vibration and the C–H out-of-plane bending vibration of the phenyl. The characteristic peak appeared at 1450 and 1418 cm^{-1} assigned to the azo group. The bands at 1369, 1315, and 1114 cm^{-1} were due to the $C–SO_2–O$ stretching vibration, the S=O stretching vibration, and the S–O– stretching vibration of the $–SO_3Na$ group, respectively [44]. After the rambutan-like $MnCo_2O_4$ microspheres adsorbed MO, the band at about 648 cm^{-1} (Co–O, typical of spinel oxide [45, 46]) shifted toward high wavenumber, and the bands at 1642 and 1074 cm^{-1} became strong, implying that an interaction exists between rambutan-like $MnCo_2O_4$ and MO. All changes in the bands before and after adsorption are consisted with the main bonds of MO. Similar phenomenon was also observed for the adsorption of methyl blue (MB) on the porous $NiFe_2O_4$ [23] and porous $MnFe_2O_4$ [24].

Adsorption kinetics of the calcined samples for methyl orange

Effect of pH values on the $MnCo_2O_4$ sorbing methyl orange

The effect of pH values on the rambutan-like $MnCo_2O_4$ sorbing methyl orange is shown in Fig. 7. The pH values have a marked effect on the adsorption degree of methyl orange in the

Fig. 5 Photograph of magnetic separation of rambutan-like $MnCo_2O_4$ obtained at 400 °C from the aqueous solution with a permanent magnet

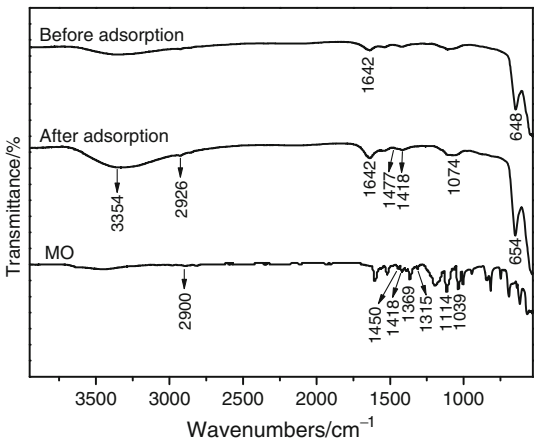

Fig. 6 FT-IR spectra of MO and the rambutan-like $MnCo_2O_4$ microspheres before and after adsorption of MO

pH range of 2–6 (Fig. 7a); the adsorption capacities of methyl orange increase with the decrease in pH values and the increase in sample calcination temperature (Fig. 7b). When solution pH value is 2.09, methyl orange concentration is 6 mg L^{-1}, and the adsorption percentage of methyl orange on the rambutan-like $MnCo_2O_4$ powder obtained at 400 °C is 93.2 % within 15 min, which shows that rambutan-like $MnCo_2O_4$ powder has a quick adsorption process for methyl orange.

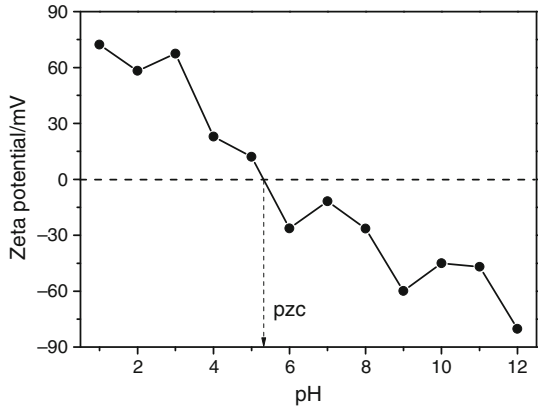

Fig. 8 Change in zeta potential of $MnCo_2O_4$ particles with change in solution pH

Figure 8 shows the zeta potentials of the dispersed $MnCo_2O_4$ particles obtained at 400 °C under different aqueous pH values. With increasing aqueous pH, the zeta potential of the $MnCo_2O_4$ decreases from positive to negative values. The pH_{PZC} value of $MnCo_2O_4$ particles is approximately 5.3. $MnCo_2O_4$ particles showed a negative charge surface (–11.75 mV) at the original pH (~7).

Adsorption kinetics with different initial methyl orange concentration

Dependence of methyl orange adsorption amount on contact time is shown in Fig. 9a. The adsorption amount q_t increases fast within initial 7 min, and then, its growth slows down. That is, the adsorption process of methyl orange on rambutan-like $MnCo_2O_4$ can be divided into rapid increase stage and the slow increase stage. The latter is also called near-equilibrium stage [31]. The rapid increase stage possibly derived from the electrostatic force between methyl orange and active adsorption sites on the surface of rambutan-like $MnCo_2O_4$. The near-equilibrium stage is attributed to the decrease in electrostatic attraction after the rambutan-like $MnCo_2O_4$ being saturated by methyl orange.

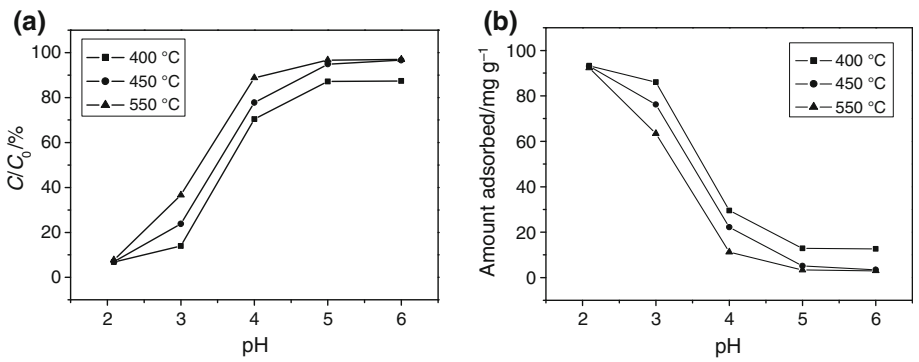

Fig. 7 Effect of pH values on the rambutan-like $MnCo_2O_4$ sorbing methyl orange: methyl orange concentration, 6 mg L^{-1}; contact time, 15 min

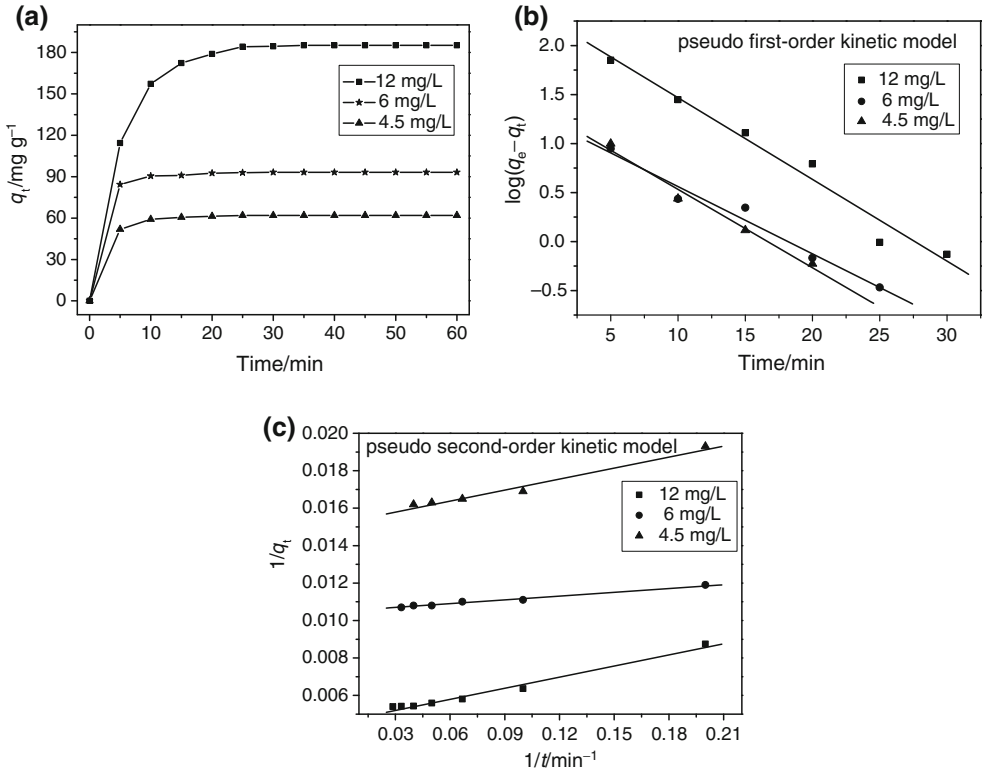

Fig. 9 Adsorption kinetics of methyl orange on rambutan-like $MnCo_2O_4$ under different initial methyl orange concentration: **a** experimental plots, **b** pseudo-first-order kinetic plots, and **c** pseudo-second-order kinetic plots (conditions: pH = 2.09; temperature = 284 K; sorbent dose = 60 mg L^{-1})

Table 1 Maximum dyes adsorption capacities of some spinel oxide adsorbents

Adsorbent	Dyes	Adsorption capacity, q_m/mg g^{-1}	References
$ZnFe_2O_4$	Acid red 88	130.6	[21]
$CuFe_2O_4$	Acid red B	86.8	[22]
$NiFe_2O_4$	Methylene blue	138.50	[23]
$NiFe_2O_4$	Methyl violet	19.06	[23]
$MnFe_2O_4$	Methylene blue	20.67	[24]
$ZnCr_2O_4$	Reactive blue 5	40.32	[27]
Fe_3O_4	Neutral red	105	[28]
$MnCo_2O_4$	Methyl orange	185.14	This work

It can also be seen that the equilibrium adsorption capacity (q_e) of methyl orange on rambutan-like $MnCo_2O_4$ increases with increasing initial methyl orange concentration. Similar phenomenon was also observed by Vadivelan [47] for methylene blue onto rice husk.

Compared to other spinel oxides (Table 1), maximum adsorption capacity q_t of MO on the rambutan-like $MnCo_2O_4$ microspheres in this work is very high. Therefore, it can be concluded that the rambutan-like $MnCo_2O_4$ microspheres is a fine adsorbent with both good adsorption capacities and good magnetic separations.

The experimental data are analyzed using the pseudo-first- and second-order adsorption kinetic models. The results are shown in Fig. 9b, c. The calculated values of the two kinetic models are shown in Table 2. The correlation coefficient of the pseudo-second-order equation is greater than that of the pseudo-first-order. Besides, experimental equilibrium adsorption amounts ($q_{e,Exp}$) are close to the theoretical values ($q_{e,Cal}$) calculated from the pseudo-second-order equation (Table 2). However, $q_{e,Exp}$ has large deviation from that of the pseudo-first-order rate equation. These results show that the adsorption mechanism of

Table 2 Parameters of the pseudo-first- and second-order kinetic models for methyl orange adsorption on $MnCo_2O_4$ under different initial methyl orange concentration

C_0/mg L^{-1}	$q_{e,Exp}$/mg g^{-1}	Pseudo-first-order equation			Pseudo-second-order equation		
		$q_{e,Cal}$/mg g^{-1}	k_{p1}/1 min^{-1}	R^2	$q_{e,Cal}$/mg g^{-1}	k_{p2}/g mg min^{-1}	R^2
4.5	61.9	21.5	0.1842	0.981	65.8	0.0133	0.981
6	93.2	17.7	0.1582	0.971	95.2	0.0172	0.982
12	185.1	200.3	0.1921	0.973	217.4	0.0015	0.981

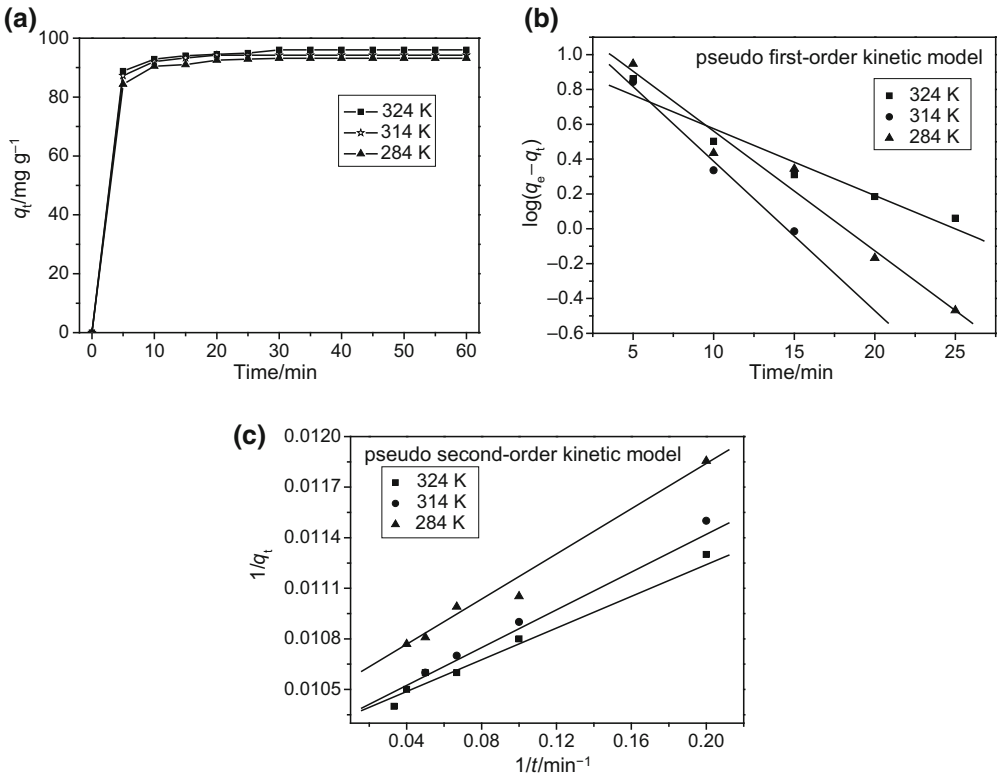

Fig. 10 Adsorption kinetics of methyl orange on rambutan-like $MnCo_2O_4$ at different temperature: **a** experimental plots, **b** pseudo-first-order kinetic plots, and **c** pseudo-second-order plots (conditions: pH = 2.09; initial methyl orange concentration = 6 mgL^{-1}; sorbent dose = 60 mg L^{-1})

methyl orange on rambutan-like $MnCo_2O_4$ most matches the pseudo-second-order kinetic models.

Adsorption kinetics at different temperature

The adsorption kinetics of methyl orange on rambutan-like $MnCo_2O_4$ at 284, 314, and 324 K are plotted in Fig. 10. From Fig. 10a, the adsorption amount of methyl orange increases with the increase in contact time, and a large fraction of methyl orange is removed within the first 5 min; the equilibrium time is about 20 min; the equilibrium adsorption amount of methyl orange is slightly improved with the increase in adsorption temperature, implying that adsorption of methyl orange on rambutan-like $MnCo_2O_4$ is an endothermic and rapid process. The adsorption kinetic curves at different temperature are analyzed with the pseudo-first- and second-order adsorption rate equations. The results are presented in Table 3. Figure 10b shows the dependence of log(q_e–q_t) on contact time; it can be seen that the pseudo-first-order equation is not applicable within the entire contact time of methyl orange adsorption on rambutan-like $MnCo_2O_4$. Figure 10c shows that the experimental plots agree well with the pseudo-second-order kinetic equation, of which the correlation coefficient is much greater than that of the pseudo-first-order kinetic equation. From Table 3, it can also be seen that the pseudo-second-order rate constant k_{p2} increases with the increase in adsorption temperature from 284 to 324 K, indicating

Table 3 Parameters of the pseudo-first- and second-order kinetic models for methyl orange adsorption on $MnCo_2O_4$ at different temperature

T/K	$q_{e,Exp}$/mg g^{-1}	Pseudo-first-order equation			Pseudo-second-order equation		
		$q_{e,Cal}$/mg g^{-1}	k_{p1}/1 min^{-1}	R^2	$q_{e,Cal}$/mg g^{-1}	k_{p2}/g mg min^{-1}	R^2
284	93.2	17.7	0.1582	0.940	95.2	0.0172	0.980
314	94.2	17.6	0.1976	0.989	97.1	0.0201	0.997
324	96.1	9.1	0.0884	0.973	97.1	0.0231	0.986

that the increase in temperature can accelerate the adsorption of methyl orange on rambutan-like $MnCo_2O_4$.

Adsorption activation energy E_a

The pseudo-second-order rate constant k_{p2}, R, and T are placed into Eq. (7) at first, and then, the dependence of ln k_{p2} on 1/T is plotted. Thus, adsorption activation energy E_a can be obtained from linear slope ($k = -E_a/R$). Figure 11 shows the dependence of ln k_{p2} on 1/T. From linear slope, the adsorption activation energy E_a is 5.71 ± 0.056 kJ mol^{-1}.

Entropy ($\Delta S^{\#}$), enthalpy ($\Delta H^{\#}$), and Gibbs energy (free enthalpy) ($\Delta G^{\#}$) of the adsorption process were calculated using Eyring equations. The results show that $\Delta S^{\#}$ and $\Delta H^{\#}$ of adsorption process are 77.60 J mol^{-1} K^{-1} and 9.30 kJ mol^{-1}, respectively. $\Delta G^{\#}$ values of the adsorption process at 284, 314, and 324 K are −12.74, −15.07, and −15.84 kJ mol^{-1}, respectively. The positive value of $\Delta H^{\#}$ indicates that the adsorption of methyl orange on rambutan-like $MnCo_2O_4$ is an endothermic process. So, the increase in temperature can increase the adsorption amount of methyl orange on rambutan-like $MnCo_2O_4$ (Fig. 10a). Usually, adsorption enthalpies ranging from 2.1 to 20.9 kJ mol^{-1} correspond to physical adsorption [48, 49]. So, the adsorption of methyl orange on rambutan-like $MnCo_2O_4$ is mechanism of physical adsorption. Based on the zeta potential analysis of the dispersed $MnCo_2O_4$ particles, $MnCo_2O_4$ particles with positive surface charge adsorb methyl orange with negative charge via electrostatic attraction. A positive ΔS value (77.60 J mol^{-1} K^{-1}) suggests an increase in the randomness at the adsorbent–solution interface during the adsorption process.

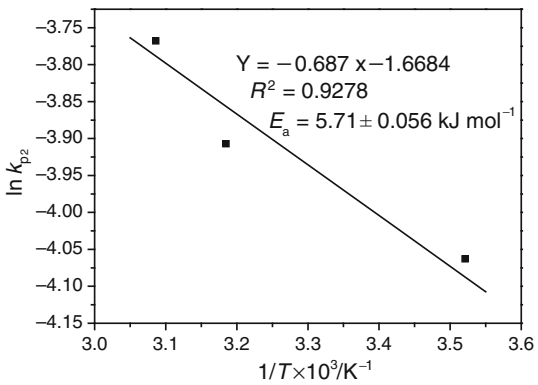

Fig. 11 Arrhenius plots for the adsorption of methyl orange on rambutan-like $MnCo_2O_4$

Conclusions

In summary, we have developed a facile and scalable co-precipitation method to fabricate the rambutan-like $MnCo_2O_4$ for the first time. The ethanol plays a key role in the formation of 3D self-assembly structure. After calcined at 400 °C in air for 10 min at a heating rate of 1 °C min^{-1}, the precursor $MnCo_2(C_2O_4)_3{\cdot}5.54H_2O$ was transformed into the rambutan-like $MnCo_2O_4$, which has the large specific surface area (155 m^2 g^{-1}) and excellent adsorption ability for methyl orange. The adsorption capacity of methyl orange on rambutan-like $MnCo_2O_4$ is 185.14 mg g^{-1} under the conditions of initial MO concentration 12 mg L^{-1} and pH 2.09, which is much higher than that of other spinel oxides for other dyes adsorption. Adsorption kinetics of methyl orange on rambutan-like $MnCo_2O_4$ follows the pseudo-second-order kinetic model. The calculated values of adsorption activation energy E_a and enthalpy $\Delta H^{\#}$ are 5.71 ± 0.056 and 9.30 kJ mol^{-1}, respectively. Methyl orange adsorption on rambutan-like $MnCo_2O_4$ is a physical adsorption process. The rambutan-like $MnCo_2O_4$ with large specific surface area also will be an excellent adsorbent for other azo dyes.

Acknowledgements This study was financially supported by the National Nature Science Foundation of China (Grant No. 21161002).

References

1. Huo YN, Xie ZL, Wang XD, Li HX, Hoang M, Caruso RA. Methyl orange removal by combined visible-light photocatalysis and membrane distillation. Dyes Pigments. 2013;98:106–12.
2. Derakhshan MS, Moradi O. The study of thermodynamics and kinetics methyl orange and malachite green by SWCNTs, SWCNT–COOH and SWCNT–NH_2 as adsorbents from aqueous solution. J Ind Eng Chem. 2014;20:3186–94.
3. Zhang P, Wang TQ, Qian GR, Wu DS, Frost RL. Removal of methyl orange from aqueous solutions through adsorption by calcium aluminate hydrates. J Colloid Interface Sci. 2014;426:44–7.

4. Haque E, Jun JW, Jhung SH. Adsorptive removal of methyl orange and methylene blue from aqueous solution with a metal-organic framework material, iron terephthalate (MOF-235). J Hazard Mater. 2011;185:507–11.
5. Chen H, Zhao J, Wu JY, Dai GL. Isotherm, thermodynamic, kinetics and adsorption mechanism studies of methyl orange by surfactant modified silkworm exuviae. J Hazard Mater. 2011;192:246–54.
6. Kou TY, Wang YZ, Zhang C, Sun JZ, Zhang ZH. Adsorption behavior of methyl orange onto nanoporous core–shell Cu@Cu_2O nanocomposite. Chem Eng J. 2013;223:76–83.
7. Semerjian L, Ayoub GM. High-pH-magnesium coagulation–flocculation in wastewater treatment. Adv Environ Res. 2003;7:389–403.
8. Ciardelli G, Corsi L, Marucci M. Membrane separation for wastewater reuse in the textile industry. Resour Conserv Recycl. 2000;31:189–97.
9. Habibi MH, Habibi AH. Photocatalytic degradation of Brilliant Red M5B using four different nanocomposites ($ZnFe_2O_4$, porous $ZnFe_2O_4$, $ZnFe_2O_4$–TiO_2, $FeTiO_3$) coated on glass. J Ind Eng Chem. 2014;20:2964–8.
10. Shirzad-Siboni M, Jafari SJ, Giahi O, Kim I, Lee SM, Yang JK. Removal of acid blue 113 and reactive black 5 dye from aqueous solutions by activated red mud. J Ind Eng Chem. 2014;20:1432–7.
11. Thinakaran N, Baskaralingam P, Pulikesi M, Panneerselvam P, Sivanesan S. Removal of acid violet 17 from aqueous solutions by adsorption onto activated carbon prepared from sunflower seed hull. J Hazard Mater. 2008;151:316–22.
12. Wang T, Su J, Jin XY, Chen ZL, Megharaj M, Naidu R. Functional clay supported bimetallic nZVI/Pd nanoparticles used for removal of methyl orange from aqueous solution. J Hazard Mater. 2013;262:819–25.
13. Guo HX, Chen JH, Weng W, Zheng ZS, Wang DF. Adsorption behavior of Congo red from aqueous solution on La_2O_3–doped TiO_2 nanotubes. J Ind Eng Chem. 2014;20:3081–8.
14. Vieira MLG, Esquerdo VM, Nobre LR, Dotto GL, Pinto LAA. Glass beads coated with chitosan for the food azo dyes adsorption in a fixed bed column. J Ind Eng Chem. 2014;20:3387–93.
15. Goscianska J, Marciniak M, Pietrzak R. Mesoporous carbons modified with lanthanum(III) chloride for methyl orange adsorption. Chem Eng J. 2014;247:258–64.
16. Yao YJ, He B, Xu FF, Chen XF. Equilibrium and kinetic studies of methyl orange adsorption on multiwalled carbon nanotubes. Chem Eng J. 2011;170:82–9.
17. Tian Y, Wang XF, Pan YF. Simple synthesis of Ni-containing ordered mesoporous carbons and their adsorption/desorption of methylene orange. J Hazard Mater. 2012;213–214:361–8.
18. Belessi V, Romanos G, Boukos N, Lambropoulou D, Trapalis C. Removal of reactive red 195 from aqueous solutions by adsorption on the surface of TiO_2 nanoparticles. J Hazard Mater. 2009;170:836–44.
19. Lv SS, Chen XG, Ye Y, Yin SH, Cheng JP, Xia MS. Rice hull/$MnFe_2O_4$ composite: preparation, characterization and its rapid microwave-assisted COD removal for organic wastewater. J Hazard Mater. 2009;171:634–9.
20. Hencl V, Mucha P, Orlikova A, Leskova D. Utilization of ferrites for water treatment. Water Res. 1995;29:383–5.
21. Konicki W, Sibera D, Mijowska E, Lendzion-Bieluń Z, Narkiewicz U. Equilibrium and kinetic studies on acid dye Acid Red 88 adsorption by magnetic $ZnFe_2O_4$ spinel ferrite nanoparticles. J Colloid Interface Sci. 2013;398:152–60.
22. Wu RC, Qu JH, He H, Yu YB. Removal of azo-dye acid red B (ARB) by adsorption and catalytic combustion using magnetic $CuFe_2O_4$ powder. Appl Catal B. 2004;48:49–56.
23. Hou XY, Feng J, Liu XH, Ren YM, Fan ZJ, Wei T, Meng J, Zhang ML. Synthesis of 3D porous ferromagnetic $NiFe_2O_4$ and using as novel adsorbent to treat wastewater. J Colloid Interface Sci. 2011;362:477–85.
24. Hou XY, Feng J, Ren YM, Fan ZJ, Zhang ML. Synthesis and adsorption properties of spongelike porous $MnFe_2O_4$. Colloids Surf A. 2010;363:1–7.
25. Xu JC, Xin PH, Gao YQ, Hong B, Jin HX, Jin DF, Peng XL, Li J, Gong J, Ge HL, Wang XQ. Magnetic properties and methylene blue adsorptive performance of $CoFe_2O_4$/activated carbon nanocomposites. Mater Chem Phys. 2014;147:915–9.
26. Yazdanbakhsh M, Khosravi I, Goharshadi EK, Youssefi A. Fabrication of nanospinel $ZnCr_2O_4$ using sol–gel method and its application on removal of azo dye from aqueous solution. J Hazard Mater. 2010;184:684–9.
27. Irama M, Guo C, Guan Y, Ishfaq A, Liu H. Adsorption and magnetic removal of neutral red dye from aqueous solution using Fe_3O_4 hollow nanospheres. J Hazard Mater. 2010;181:1039–50.
28. Kong LB, Lu C, Liu MC, Luo YC, Kang L, Li XH, Walsh FC. The specific capacitance of sol–gel synthesised spinel $MnCo_2O_4$ in an alkaline electrolyte. Electrochim Acta. 2014;115:22–7.
29. Zhu JK, Gao QM. Mesoporous MCo_2O_4 (M = Cu, Mn and Ni) spinels: structural replication, characterization and catalytic application in CO oxidation. Microporous Mesoporous Mater. 2009;124:144–52.
30. Wang KT, Wu XH, Wu WW, Hu YM, Liao S. Synthesis of spinel $MnCo_2O_4$ by thermal decomposition of carbonates and kinetics of thermal decomposition of precursor. J Supercond Nov Magn. 2014;27:1249–56.
31. Cao W, Dang Z, Yuan BL, Shen CH, Kan J, Xue XL. Sorption kinetics of sulphate ions on quaternary ammonium-modified rice straw. J Ind Eng Chem. 2014;20:2603–9.
32. Arias F, Kanti Sen T. Removal of zinc metal ion (Zn^{2+}) from its aqueous solution by kaolin clay mineral: a kinetic and equilibrium study. Colloids Surf A. 2009;348:100–8.
33. Wu HB, Pang H, Lou XW. Facile synthesis of mesoporous $Ni_{0.3}Co_{2.7}O_4$ hierarchical structures for high-performance supercapacitors. Energy Environ Sci. 2013;6:3619–26.
34. Qiu H, Lv L, Pan BC, Zhang QJ, Zhang WM, Zhang QX. Critical review in adsorption kinetic models. J Zhejiang Univ Sci A. 2009;10:716–24.
35. Qu R, Wang M, Song R, Sun C, Zhang Y, Sun X, Ji C, Wang C, Yin P. Adsorption kinetics and isotherms of Ag(I) and Hg(II) onto silica gel with functional groups of hydroxyl- or amino-terminated polyamines. J Chem Eng Data. 2011;56:1982–90.
36. Ho YS, McKay G. Pseudo-second order model for adsorption processes. Process Biochem. 1999;34:451–65.
37. Ptáček P, Opravil T, Šoukal F, Havlica J, Másilko J, Wasserbauer J. Preparation of dehydroxylated and delaminated talc: Meta-talc. Ceram Int. 2013;39:9055–61.
38. Vlaev L, Nedelchev N, Gyurova K, Zagorcheva M. A comparative study of non-isothermal kinetics of decomposition of calcium oxalate monohydrate. J Anal Appl Pyrolysis. 2008;81:253–62.
39. Qin LQ, Gao ML, Wu WW, Ou SQ, Wang KT, Liu B, Wu XH. $Co_{1-x}Mg_xFe_2O_4$ magnetic particles: preparation and kinetics research of thermal transformation of the precursor. Ceram Int. 2014;40:10857–66.
40. Zhou KW, Wu WW, Li YN, Wu XH, Liao S. Preparation of magnetic nanocrystalline $Mn_{0.5}Mg_{0.5}Fe_2O_4$ and kinetics of thermal decomposition of precursor. J Therm Anal Calorim. 2013;114:205–12.
41. Chen Y, Song BH, Li M, Lu L, Xue JM. Fe_3O_4 nanoparticles embedded in uniform mesoporous carbon spheres for superior high-rate battery applications. Adv Funct Mater. 2014;24:319–26.

42. Li J, Xiong S, Li X, Qian Y. A facile route to synthesize multiporous $MnCo_2O_4$ and $CoMn_2O_4$ spinel quasi-hollow spheres with improved lithium storage properties. Nanoscale. 2013;5:2045–54.
43. Li L, Zhang YQ, Liu XY, Shi SJ, Zhao XJ, Zhang H, Ge X, Cai GF, Gu CD, Wang XL, Tu JP. One-dimension $MnCo_2O_4$ nanowire arrays for electrochemical energy storage. Electrochim Acta. 2014;116:467–74.
44. Zhang Z, Wu ZL, Liu GM. Interfacial adsorption of methyl orange in liquid phase of foam fractionation using dodecyl dimethyl betaine as the collector. J Ind Eng Chem. 2015;. doi:10.1016/j.jiec.2015.01.027.
45. Wu XH, Zhou KW, Wu WW, Cui XM, Li YN. Magnetic properties of nanocrystalline $CuFe_2O_4$ and kinetics of thermal decomposition of precursor. J Therm Anal Calorim. 2013;111:9–16.
46. Zhang YT, Liu SA, Li Y, Deng DM, Si XJ, Ding YP, He HH, Luo LQ, Wang ZX. Electrospun graphene decorated $MnCo_2O_4$ composite nanofibers for glucose biosensing. Biosens Bioelectron. 2015;66:308–15.
47. Vadivelan V, Vasanth Kumar K. Equilibrium, kinetics, mechanism, and process design for the adsorption of methylene blue onto rice husk. J Colloid Interface Sci. 2005;286:90–100.
48. Belala Z, Jeguirim M, Belhachemi M, Addoun F, Trouve G. Biosorption of basic dye from aqueous solutions by date stones and palm-trees wastes: kinetic, equilibrium and thermodynamic studies. Desalination. 2011;271:80–7.
49. Gong R, Ye JJ, Dai W, Yan XY, Hu J, Hu X, Li S, Huang H. Adsorptive removal of methyl orange and methylene blue from aqueous solution with finger-citron-residue-based activated carbon. Ind Eng Chem Res. 2013;52:14297–303.